

Linearity Characterization and Uncertainty Quantification of Spectroradiometers via Maximum Likelihood and the Non-parametric Bootstrap

A L Pintar¹, Z H Levine², H W Yoon³, S E Maxwell³

¹ Statistical Engineering Division, National Institute of Standards and Technology, Gaithersburg, Maryland 20899-8980 USA; apintar@nist.gov

² Quantum Measurement Division, National Institute of Standards and Technology, Gaithersburg, Maryland 20899-8441 USA; zlevine@nist.gov

³ Sensor Science Division, National Institute of Standards and Technology, Gaithersburg, Maryland 20899-8441 USA; smaxwell@nist.gov

Abstract. A rigorous uncertainty quantification for “flux-addition,” (also known as the “combinatoric technique”) a well-known technique in the radiometry field, is investigated. A probabilistic model for digital readings at given fluxes and values of polynomial coefficients describing the nonlinear instrument response is proposed. Maximum likelihood estimates (MLEs) of the unknown fluxes and polynomial coefficients are recommended. A non-parametric bootstrap algorithm is introduced to quantify uncertainty, e.g., to calculate standard errors. The model and bootstrap algorithm are studied by simulation. These simulation are performed using fluxes and polynomial coefficients consistent with those observed during the characterization of the Orbiting Carbon Observatory-2, for each of its focal planes. The MLEs are found to be approximately unbiased, and confidence intervals derived from the bootstrap replicates are found to be consistent with their target coverage of 95 %. For the polynomial coefficients representing the linearization function, the relative bias was less than 1 % and the observed coverages range from 90 % to 97 %. An experimental data set from the NIST Beam Conjoiner, which implements flux addition with a broadband light-source and a set of neutral density filters, is also considered. In this example, a complete calibration is generated assuming that one flux level is well characterized by the spectroradiometer. The uncertainty contribution attributable to estimation of the instrument’s nonlinear response is less than 0.02 % over most of its range.

Keywords: Satellite Based Measurements, Spectroradiometer, Calibration, Maximum Likelihood, Bootstrap

1. Introduction

Almost all indicating instruments and their attached sensors require calibrations so that their responses to external stimuli can be converted to quantitative measurement units. However, oftentimes the calibrations of these instruments can only be performed at just a single or few values when their sensitivity can range over many orders of magnitude. Thus in the calibration of indicating instruments, the linearity of the instrument is often

of particular interest. If an instrument’s response has been perfectly linearized, only a single known non-zero stimulus is required for calibration. One method for assessing linearity is the “flux-addition” method or the “combinatorial technique.”

The flux-addition method is frequently used in the calibration of many types of instruments [1]. Briefly, the technique exploits the property of a linear function $f(a + b) = f(a) + f(b)$ to construct a system of equations that enables the recovery of the response function of an indicating instrument up to an overall scaling factor using a set of unknown stimuli.

A common technique for recovering the response function involves assuming a polynomial form for it, then setting up a system of equations that includes both the coefficients of the polynomial and the unknown stimuli. This system can be solved using either pseudoinverse methods or any number of numerical optimization routines. However, because both the stimuli and the response function are unknown, additional constraints are needed to obtain a unique solution. We know of no published standard method to recover meaningful uncertainty statements about the estimated parameters, e.g., confidence intervals, in this setting. Here, we develop a maximum likelihood inversion technique that, in concert with a bootstrap algorithm, may be used as part of a full uncertainty analysis when calibrating an indicating instrument. We then apply this technique to two systems. The first system is a simulation of a light source similar to that used in calibrations of Earth observing satellites, and the second system is NIST’s optical Beam Conjoiner [2].

In the simulation, we make a direct comparison of the recovered parameters to the known inputs, enabling an evaluation of the algorithm’s performance. We also explain how in the case of flux calibrations, a linear calibration may be achieved even in the presence of non-uniform illumination, which is a critical problem in the calibration of remote sensing instruments. In the application to the Beam Conjoiner, we compare the results of the new method to the results obtained using the traditional inversion technique. We also show how uncertainty in the estimated nonlinear detector response can be incorporated into a calibration using the output from the bootstrap algorithm.

The remainder of the article is organized as follows: Section 2 describes the probabilistic model and techniques used to estimate the fluxes and polynomial coefficients as well as quantify uncertainty in those estimates. Section 3 presents the results of a simulation study using realistic assumptions based on NIST’s experience calibrating earth observing satellites. Section 4 presents results for an experimental data set collected at NIST using the Beam Conjoiner and a commercial spectroradiometer. Finally, Section 5 summarizes the main contributions of the article.

2. Methodology

Assume that an indicating instrument reading of a digital number is denoted by the symbol n , and that the stimulus producing the reading n is Φ . In other literature, n has sometimes been referred to by the symbol DN . An instrument has a linear response

when $n \propto \Phi$ (ignoring bias and electronic noise for the moment). It is often the case that $n = h(\Phi)$, with h some monotonic, continuous function. In this case, it is of interest to find h^{-1} so that $h^{-1}(n) = \Phi$. Often the linearizing function, h^{-1} , is approximated by a polynomial,

$$h^{-1}(n) = \beta_0 + \sum_{m=1}^p \beta_m n^m,$$

with $p \leq 5$. Other functional forms, including splines, may be assumed and incorporated into this method, but for concreteness we only consider the polynomial functions.

It is the goal of a calibration to estimate the coefficients $\beta = (\beta_0, \dots, \beta_p)$. To accomplish this, the lead of [1] may be followed. The method is called the combinatoric technique or, in the case of radiometric calibrations, the flux-addition or the Beam Conjoiner method. The technique may be used to determine both the stimuli that the instrument observes as well as the coefficients. Up to the overall scaling, no prior knowledge of the stimuli is required. The output of the technique is a scaled measurement of the fluxes that includes variation across footprints as well as the polynomial coefficients. A single measurement of a uniform, known flux may then be incorporated to determine the scaling factor and to produce a measurement of any flux.

2.1. Statistical Model

The linearizing function, h^{-1} may be estimated using the flux addition method with an integrating sphere source. In contrast to [3], which uses two light sources, we consider an integrating sphere with $J > 2$ lamps. The number of combinations is 2^J . A probabilistic model can be used to express the 2^J detector readings as a function of the individual lamp fluxes, nonlinear detector response, and electronic noise. Using only the detector readings and knowledge of the lamp configurations (i.e., its off/on pattern), it is not possible to estimate both the individual lamp fluxes and the nonlinear detector response. Additional constraints are necessary, and are described as a part of the probabilistic model. The model is

$$\begin{aligned} n_i &\sim \text{Normal} \left(\alpha_0 + \sum_{m=1}^p \alpha_m P_m(s(\Phi_i)), \sigma^2 \right) \\ \Phi_i &= \sum_j x_{ij} \phi_j \\ \sum_j \phi_j &\sim \text{Normal}(\Phi_{\max}, \tau^2) \\ \alpha_1 &\sim \text{Normal} \left(\frac{\Phi_{\max}}{2}, \gamma^2 \right) \\ \alpha_m &\sim \text{Normal}(0, \gamma^2) \text{ for } m > 1 \\ \gamma &\sim \text{Exponential}(\lambda). \end{aligned} \tag{1}$$

In Equation (1), n_i is the instrument reading from experimental run i , Φ_i is the flux for experimental run i , s is a linear transformation of Φ_i to the interval $[-1, 1]$, P_m

is the Legendre polynomial of order m [4], $\boldsymbol{\alpha} = (\alpha_0, \dots, \alpha_p)$ is a vector of polynomial coefficients, ϕ_j is the flux of lamp j , x_{ij} takes the values 0 or 1 for lamp j being off or on in experimental run i , σ represents electronic noise, Φ_{\max} estimates the maximum flux (and so sets the overall flux scale), τ represents the standard deviation associated with knowledge of the maximum flux, γ is a penalty parameter that pulls the regression coefficients towards expected values *a priori*, and λ is another penalty parameter that disallows very large values of γ . In Equation (1), the n_i , the x_{ij} , Φ_{\max} , τ , and λ are taken to be known fixed quantities. All other parameters in Equation (1), i.e., $\boldsymbol{\phi} = (\phi_1, \dots, \phi_J)$, $\boldsymbol{\alpha}$, γ , and σ are realized as maximum likelihood estimates (MLEs) (see for example Chapters 4 and 5 of [5]).

The constraints $\sum_j \phi_j \sim \text{Normal}(\Phi_{\max}, \tau^2)$, $\alpha_1 \sim \text{Normal}(\frac{\Phi_{\max}}{2}, \gamma^2)$, and $\alpha_m \sim \text{Normal}(0, \gamma^2)$ for $m > 1$ in Equation (1) are crucial to decoupling the lamp fluxes from the nonlinear response of the detector. Without any of these constraints, the estimation problem is ill-posed. It is possible, using data from a separate experiment, to know the values of Φ_{\max} and τ . The linear coefficient α_1 is coerced toward $\frac{\Phi_{\max}}{2}$ because the light levels Φ_i would naturally lie in the interval $[0, \Phi_{\max}]$, and over that interval, the linear coefficient is expected to be near one. Since Legendre polynomials are orthogonal in the interval $[-1, 1]$, the interval $[0, \Phi_{\max}]$ is shifted and scaled to the interval $[-1, 1]$, and a slope of one on the original interval is a slope of $\frac{\Phi_{\max}}{2}$ on the new interval. The higher order coefficients are coerced toward zero because the linear coefficient is expected to dominate.

Coercing polynomial coefficients towards meaningful values, to balance prediction variance and bias, resembles the technique known as ridge regression, introduced originally in [6], and the technique known as LASSO (for “Least Absolute Shrinkage and Selection Operator”), originally introduced in [7]. Since the Gaussian distribution is leveraged to achieve the coercion, the similarity to ridge regression is more striking. It also resembles standard Bayesian treatments of regression problems, see for example Section 14.8 of [8], which uses Gaussian prior distributions for regression coefficients, and [9] which uses Laplace prior distributions.

The statistical model requires stability in the spatial patterns of the integrating sphere and in the repeatability of lamp flux levels over the duration of the acquisition of the n_i . That requirement is reflected in Equation (1) by the fact that the lamp fluxes, the ϕ_j , do not change across experimental runs. However, integrating spheres have variable throughput that depends on the average reflectance of the interior surface. In Section 3, the effects of variable throughput on the MLEs are examined.

Up to constant terms, the log-likelihood function corresponding to Equation (1) is

$$\begin{aligned} \ell(\boldsymbol{\Phi}, \boldsymbol{\alpha}, \gamma, \sigma) = & -\frac{1}{2\sigma^2} \left[\sum_{i=1}^N \left(n_i - \alpha_0 - \sum_{m=1}^p \alpha_m P_m(s(\Phi_i)) \right)^2 \right] - \\ & N \log \sigma - \frac{1}{2\tau^2} \left(\sum_{j=1}^J \phi_j - \Phi_{\max} \right)^2 - \end{aligned}$$

$$\begin{aligned} & \frac{1}{2\gamma^2} \left(\alpha_1 - \frac{\Phi_{\max}}{2} \right)^2 - \log \gamma - \\ & \frac{1}{2\gamma^2} \left[\sum_{m=2}^p (\alpha_m)^2 \right] - (p-1) \log \gamma - \lambda \gamma. \end{aligned} \quad (2)$$

2.2. Variable Apertures

As was used to calibrate the Orbiting Carbon Observatory-2 [10], we make one of the lamps a variable aperture. Assume there are J lamps, and without loss of generality, assume the variable aperture lamp is lamp J . Modify Φ_i as follows:

$$\Phi_i = \sum_{j=1}^J x_{ij} \phi_j + \sum_{k=1}^{N_v} x_{iJk} \psi_k \phi_J$$

where the ψ_k are constants in $[0,1]$ to be estimated, the x_{iJk} are indicator variables that take values 0 and 1, and $\boldsymbol{\psi} = (\psi_1, \dots, \psi_{N_v})$. At most one of $x_{iJ}, x_{iJ1}, \dots, x_{iJN_v}$ is 1, but they can all be 0. Consider an example with $N_v = 3$. The vector $(0, 0, 0, 0)$ represents lamp J being completely off, $(1, 0, 0, 0)$ represents lamp J being on at full power, $(0, 1, 0, 0)$, represents lamp J being on at the lowest of the three variable settings, and so on.

A detail of integrating spheres is left out of our model for simplicity. The detail is that an integrating sphere is a diffuse optical cavity whose throughput will change depending when it is loaded by opening and closing shutters. Experience with one particular integrating sphere used in [11] indicates that this effect is at the 0.1 % level, and it can be accommodated by multiplying the fluxes ϕ_j with a configuration factor that is experimentally determined. The experimental determination would be done by turning on a single lamp and measuring flux changes as other shutters are opened and closed.

2.3. Linearization Function

The model in Equation (1) is a forward model in the sense that for given values of the lamp fluxes, the polynomial coefficients, and the electronic noise, the probability distribution for the instrument signal is fixed. However, the goal of calibration in this context is to predict the flux viewed by the detector corresponding to the instrument response. Calibration is fully treated in Section 4.3, but a first step is linearizing the instrument reading which is achieved by inverting the polynomial equation $E[n] = \alpha_0 + \sum_{m=1}^p \alpha_m P_m(s(\Phi))$, where $E[n]$ is the expected instrument reading for the flux Φ . The inverse function is approximated by a series of monomials (instead of Legendre polynomials) up to degree p . Specifically,

$$\Phi = \beta_0 + \sum_{m=1}^p \beta_m E[n]^m. \quad (3)$$

To estimate the parameters β_0, \dots, β_p , from $\alpha_0, \dots, \alpha_p$, a regular sequence of values is constructed over the interval $[-1, 1]$ and transformed by s^{-1} , the inverse of the

linear transformation s . Denote this sequence $\hat{\Phi}_\ell$, with $\ell = 1, \dots, L$. The maximum likelihood estimates of $\alpha_0, \dots, \alpha_p$ are $\hat{\alpha}_0, \dots, \hat{\alpha}_p$, and we construct $E[\hat{n}_\ell] = \hat{\alpha}_0 + \sum_{m=1}^p \hat{\alpha}_m P_m(s(\hat{\Phi}_\ell))$. Finally, ordinary least squares is used to estimate $\beta = (\beta_0, \dots, \beta_p)$ by minimizing $\sum_{\ell=1}^L \left(\hat{\Phi}_\ell - \beta_0 - \sum_{m=1}^p \beta_m E[\hat{n}_\ell]^m \right)^2$. The estimate is $\hat{\beta} = (\hat{\beta}_0, \dots, \hat{\beta}_p)$.

2.4. Uncertainty

Uncertainty for all parameters is quantified by a bootstrapping pairs approach [see Section 7.2 and 9.5 in Ref. 12, for example]. A bootstrap sample of the same size as the original dataset is generated by sampling with replacement pairs of (n_i, \mathbf{x}_i) , where $\mathbf{x}_i = (x_{i1}, \dots, x_{iJ}, x_{iJ1}, \dots, x_{iJN_v})$. Bootstrap sample b , of pairs, is denoted $\{(n_i^{*,b}, \mathbf{x}_i^{*,b})\}_{i=1}^n$. For each bootstrap sample, the maximum likelihood estimate of ϕ , α , γ , σ , ψ , and β is calculated, and for bootstrap sample b , call them $\phi^{*,b}$, $\alpha^{*,b}$, $\gamma^{*,b}$, $\sigma^{*,b}$, $\psi^{*,b}$, and $\beta^{*,b}$. The collection of bootstrap replicates of the maximum likelihood estimates $\{(\phi^{*,b}, \alpha^{*,b}, \gamma^{*,b}, \sigma^{*,b}, \psi^{*,b}, \beta^{*,b})\}_{b=1}^B$ may be used to estimate standard errors and calculate confidence intervals. For example, the standard error (se) of $\hat{\beta}_1$ may be approximated as $\text{se}[\hat{\beta}_1] = \sqrt{\frac{\sum_{b=1}^B (\beta_1^{*,b} - \bar{\beta}_1^{*,\cdot})^2}{B-1}}$ where $\bar{\beta}_1^{*,\cdot} = \frac{1}{B} \sum_{b=1}^B \beta_1^{*,b}$. A 95 % confidence interval for β_1 is of the form [lb, ub] where lb is the 2.5 %-ile and ub is the 97.5 %-ile of $\{\beta_1^{*,b}\}_{b=1}^B$.

The bootstrap algorithm accounts for sampling variability, i.e., how much the maximum likelihood estimates might change if the experiment were repeated under identical conditions, but it does not account for other sources of uncertainty like model uncertainty, i.e., the mismatch between the model and reality. One potential mismatch is that the model in Equation (1) assumes that the ϕ_j , $j = 1, \dots, J$ are constant throughout the experiment. If the fluxes of the lamps drift during the experiment, this is not true, but it may be accounted for in the bootstrap algorithm by also randomly perturbing Φ_{\max} for each bootstrap sample. In this work, two cases are considered, the lamps drift independently of each other, and they drift together identically. These two cases represent the two possible extremes.

Assume momentarily that the ϕ_j in Equation (1) are random variables instead of fixed but unknown parameters to be estimated. Then, we may think of calculating $\text{Var} \left[\sum_j \phi_j \right]$. In the independent case, $\text{Var} \left[\sum_j \phi_j \right] = \sum_j \text{Var}[\phi_j]$. In the case that the lamps drift identically together, $\text{Var} \left[\sum_j \phi_j \right] = J^2 \text{Var}[\phi_1]$. To account for the possibility that the lamps drift during the experiment, Φ_{\max} in Equation (1) is perturbed by Gaussian white noise with variance $\text{Var} \left[\sum_j \phi_j \right]$ for each bootstrap iteration. This can work well even if the individual lamps drift according to a distribution other than a Gaussian distribution because the assumption of Gaussian drift is placed on the sum of the lamp fluxes, which by the central limit theorem may be reasonable even if the individual lamps drift according to a different distribution. The value of $\text{Var} \left[\sum_j \phi_j \right]$ is an input to the analysis procedure, and it is similar to a prior distribution in Bayesian inference. It must be based either on subject matter expertise or on data collected

ID	identical lamps	linear drift	correlated drifts
1	✓	0 %	NA
2	✓	0.5 %	✗
3	✓	0.5 %	✓
4	5 % differences	0.5 %	✓

Table 1: The four conditions considered in the simulation study. NA means “not applicable.”

externally to the calibration experiment.

3. Simulation Study

The methodology described in Section 2 was tested using simulated data under four conditions of practical interest, listed in Table 1. For each condition, 100 sets of instrument readings, the n_i , were generated. For each set of n_i , the methodology of Section 2 was applied, and the results compared to the known ground truth. The comparisons are presented in Section 3.2. The generation of the sets of instrument readings are discussed next.

3.1. Signal Simulation

To generate one set of n_i , the values of x_{ij} and x_{iJk} are first defined, representing the lamp configurations. The number of lamps is taken to be $J = 7$. One lamp has a variable aperture and the number of variable aperture positions $N_v = 3$ is used. These choices are arbitrary but are similar to values on existing spheres used for calibration of remote sensing instruments [13, 10]. For the six lamps that do not have a variable aperture, there are $2^6 = 64$ possible off/on configurations. The variable aperture lamp can take on 5 possible states, off, on at full intensity, or on at one of the three intensities that are lower than full intensity. This gives $64 \times 5 = 320$ possible lamp configurations. Each simulated data set contains all 320 possible lamp configurations, plus five repeats with all lamps off, and five repeats with all lamps on at full intensity, giving a total of 330 lamp configurations in each simulated data set.

Next, values are chosen for the ϕ_j , $j = 1, \dots, 7$, ψ_k , $k = 1, \dots, 3$, and β_0, \dots, β_p . In all simulations, $p = 3$, $\psi_1 = 0.25$, $\psi_2 = 0.5$, $\psi_3 = 0.75$, $\beta_0 = 0.5$, $\beta_1 = 1$, $\beta_2 = 0.022$, and $\beta_3 = -0.008$. For simulation 1, where the lamps are identical and do not drift, $\phi_j = \frac{1}{7}$, $j = 1, \dots, 7$. For simulation 2, the ϕ_j drift experimental-run-to-experimental-run, at most 0.5 % from $\frac{1}{7}$, and they drift independently of each other. For simulation 3, the ϕ_j also drift at most 0.5 % from $\frac{1}{7}$, but within an experimental run, they drift identically. That is, if for experimental run 1, $\phi_1 = 0.001 \times \frac{1}{7}$, it is also the case that $\phi_2 = 0.001 \times \frac{1}{7}$. For simulation 4, the ϕ_j are randomly selected to be within approximately 2.5 % of $\frac{1}{7}$, subject to a sum to unity constraint. For simulation 4, the ϕ_j also drift at most 0.5 %

between experimental runs, and they do so identically within an experimental run.

Given values for all of the x_{ij} , x_{iJk} , ϕ_j , and ψ_k , $\Phi_i = \sum_j^J x_{ij}\phi_j + \sum_k^{N_v} x_{iJk}\psi_k\phi_J$. Then, Φ_i is perturbed by Gaussian white noise with standard deviation $1.1 \times 10^{-4}\sqrt{\Phi_i}$ (shot noise) yielding $\tilde{\Phi}_i$. This value is for illustrative purposes; a real-world application may require tuning of the noise model, as is done in Section 4.

Given values for all of the β_m , \tilde{n}_i is obtained by solving the equation

$$\tilde{\Phi}_i = \beta_0 + \sum_{m=1}^p \beta_m \tilde{n}_i^m.$$

On physical grounds we expect the relation between the observations \tilde{n}_i and $\tilde{\Phi}_i$ to be monotonic: a greater flux leads to a greater signal even in the presence of nonlinearity. Hence, there is a unique real solution. Finally, Gaussian white noise (electrical noise) with standard deviation 10^{-3} is added to the \tilde{n}_i to yield n_i .

3.2. Results

Figure 1 shows the simulation results for β_0 , β_1 , β_2 , and β_3 for 100 simulated data sets for each of the 4 simulation scenarios described in Table 1. The points are the MLEs ordered from smallest to largest, and the lines (which are difficult to distinguish individually) are 95 % confidence intervals. The black vertical lines are the true values, and the numbers to the right are the proportion of confidence intervals that bracket the true value, the target being 0.95. From Figure 1, it can be seen that the true values of β_0 , β_1 , β_2 , and β_3 , lie around the center of the 100 maximum likelihood estimates for each scenario. This implies that the estimation procedure is approximately unbiased. To put it another way, the true values are approximately equal to the estimates, on average. For β_0 and β_1 , for the 100 simulations pictured, the observed relative bias is less than 0.1 %. For β_2 and β_3 , it is less than 1 %.

Also from Figure 1, it may be seen that the bootstrap procedure described in Section 2.4 achieves its nominal coverage of 95 % for β_0 , β_1 , β_2 , and β_3 . This claim is tenable even though none of the values on the right side of Figure 1 are exactly 0.95. Because of the finite number (namely, 100) of simulations for each scenario, 1 of the 16 proportions in Figure 1 is expected to lie outside of the interval (0.91, 0.99) even if the true coverage is exactly 95 %, which is indeed the case. Another important observation from Figure 1 is that for β_0 and β_1 the confidence intervals are shortest for simulation scenario 1, and longest for scenarios 3 and 4. This occurs because of the extra uncertainty introduced into the bootstrap algorithm that is intended to account for lamp drift during the experiment. The widths of the confidence intervals for scenario 2 are in between the two extremes of perfectly correlated drift between the lamps in scenarios 3 and 4 and no drift in scenario 1. The widths of the confidence intervals for β_2 and β_3 do not vary systematically between the simulation scenarios, implying that uncertainty for those higher order coefficients is primarily due to sampling variability not lamp drift.

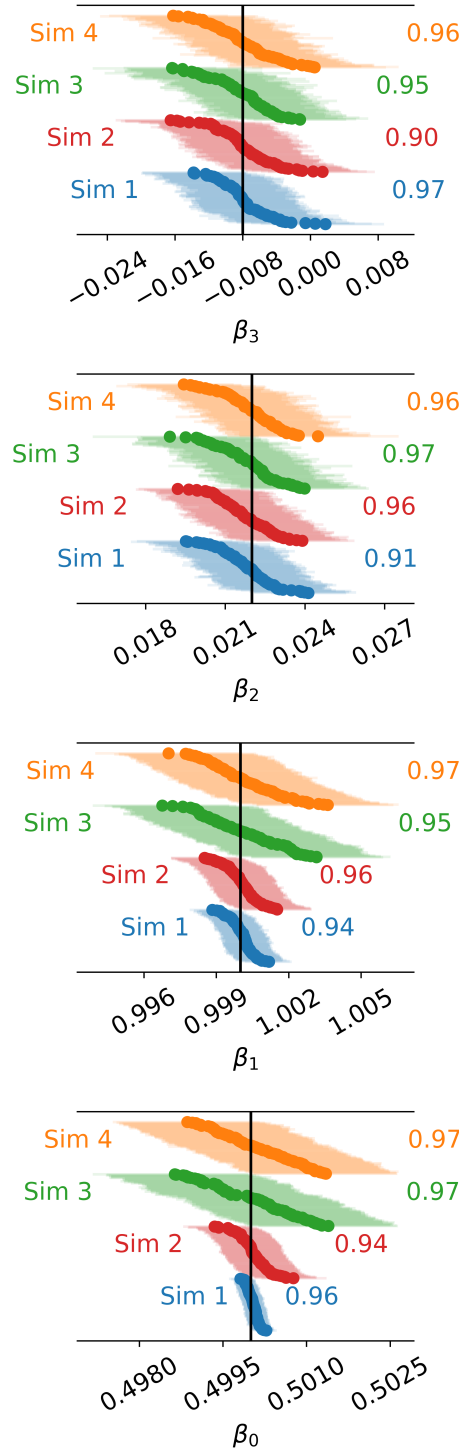


Figure 1: Results for β_0 , β_1 , β_2 , and β_3 for 100 simulated data sets for each of the 4 simulation scenarios described in Table 1. The points are the MLEs ordered from smallest to largest, and the lines (which are difficult to individually distinguish) are 95 % confidence intervals. The black vertical lines are the true values, and the numbers to the right are the proportion of confidence intervals that bracket the true value.

Figure 2 shows similar results as in Figure 1, but for ψ_1 , ψ_2 , and ψ_3 . Again, the true values are centered around the 100 maximum likelihood estimates, implying that the estimators are unbiased. The observed relative biases are less than 0.2 %. Further, the coverage proportion of the confidence intervals is consistent with the nominal 95 %. In Figure 2, it is also observed that the widths of the confidence intervals between simulation scenarios are similar. As with β_2 and β_3 , this implies that the dominant component of uncertainty for ψ_1 , ψ_2 , and ψ_3 is sampling variability, not lamp drift.

Figure 3 is similar to Figures 1 and 2, but for ϕ_1, \dots, ϕ_7 . Simulation scenario 4 is not plotted because lamps are not assumed to be nominally identical as in scenarios 1, 2, and 3. Again, the true average lamp fluxes are centered about the 100 maximum likelihood estimates, implying no bias. The observed relative biases are less than 0.1 %. On the other hand, for scenarios 2 and 3, the coverage proportions of the confidence intervals are not consistent with the nominal 95 %. This occurs because the lamp fluxes are not exactly $\frac{1}{7}$, but instead drift around $\frac{1}{7}$ during the experiment. The deviation of the coverage proportions from the nominal coverage for ϕ_1, \dots, ϕ_7 when the lamps drift is not concerning since the modified bootstrap algorithm accounts for the variation due to drift through Φ_{\max} , which affects the individual ϕ_j only indirectly through their sum.

The simulation scenarios considered here show that the maximum likelihood estimation procedure and the non-parametric bootstrap algorithm work well for estimating nonlinear detector response as well as variable lamp intensities. For the scenarios where the lamps do not drift during the experiment, the procedures also work well for estimating the true lamp intensities. The only cases for which the bootstrap algorithm did not convey good estimates of the uncertainty were simulation scenarios 2 and 3 (and 4, although not presented) for the true lamp intensities, ϕ_1, \dots, ϕ_7 . In those scenarios, the lamps are assumed to drift during the experiment, and so in reality there is no single true value to compare the estimate lamp intensity to. Thus, we do not find it concerning that the coverage proportions for the bootstrap confidence intervals are not consistent with the target 95 %. The value $\frac{1}{7}$ may not have been the correct target for ϕ_j for any one of the simulations, but on average, it was the correct target. Even in the case of drifting lamps, the maximum likelihood estimates remain unbiased because as expected, over 100 simulations, the average lamp intensity, $\frac{1}{7}$, falls in the center of them.

4. Application to the Beam Conjoiner

The procedures of Section 2 are now applied to an experimental data set from the Beam Conjoiner, which is described in detail in [2] and briefly here, and compared to the currently employed technique for analyzing the data from those experiments. The Beam Conjoiner comprises a light source (typically a single quartz tungsten halogen lamp) whose output is collimated and split along two different paths. The resulting beams pass through independent neutral density filter wheels, and then are combined once again and the combined beam passes through a third, shared, neutral density filter

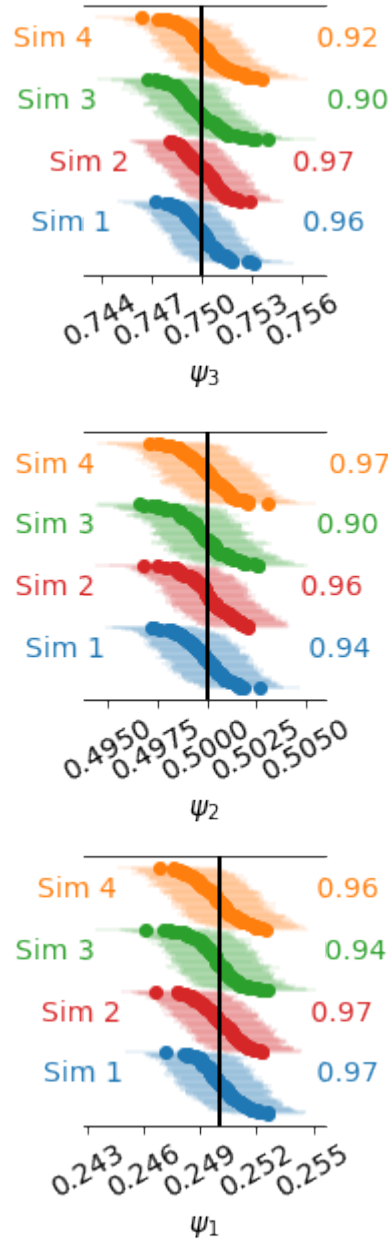


Figure 2: Results for ψ_1 , ψ_2 , and ψ_3 for 100 simulated data sets for each of the 4 simulation scenarios described in Table 1. The points are the MLEs ordered from smallest to largest, and the lines (which are difficult to individually distinguish) are 95 % confidence intervals. The black vertical lines are the true values, and the numbers to the right are the proportion of confidence intervals that bracket the true value, the target being 0.95.

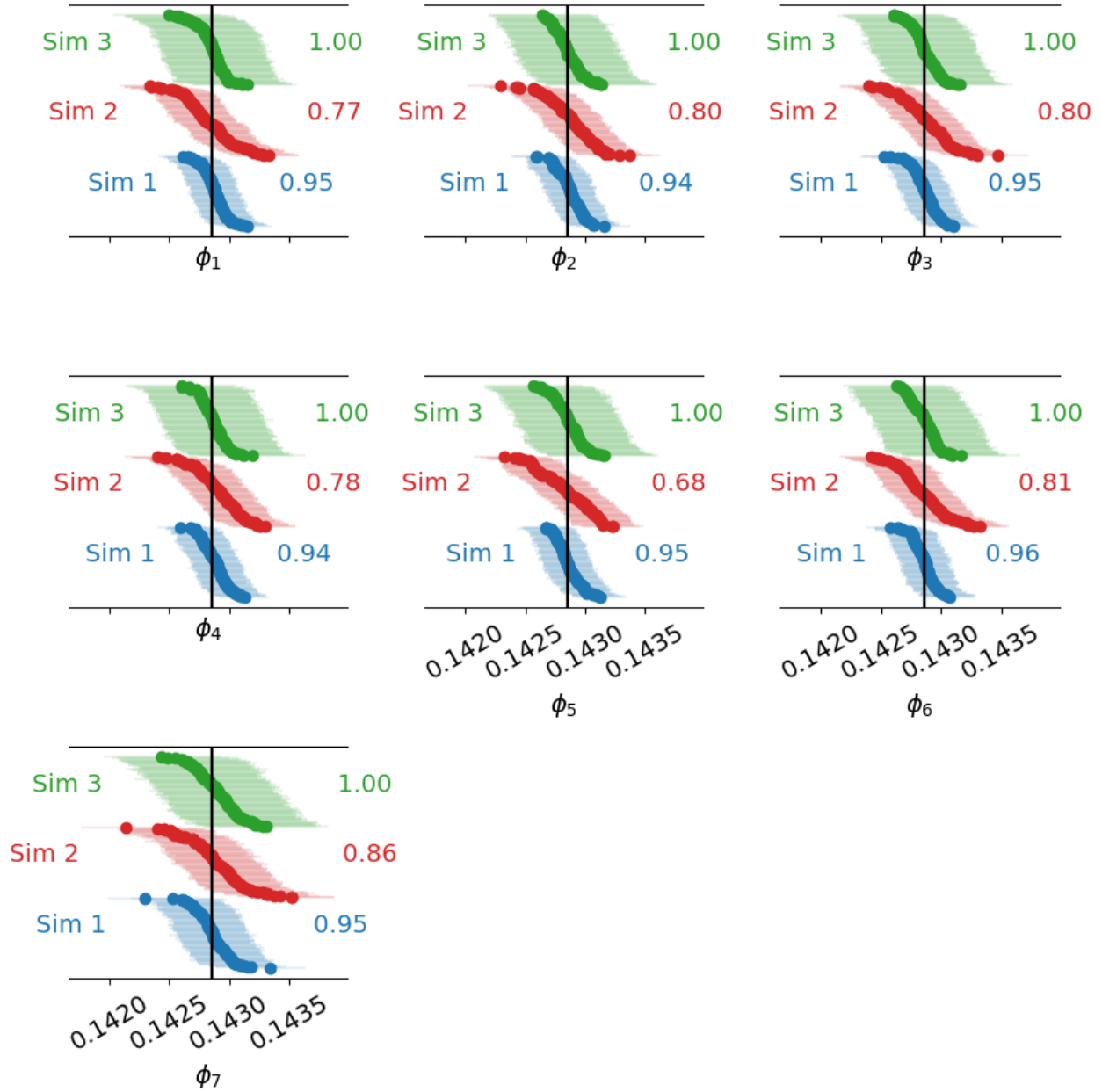


Figure 3: Results for ϕ_1, \dots, ϕ_7 for 100 simulated data sets for the first 3 of 4 simulation scenarios described in Table 1. The points are the MLEs ordered from smallest to largest, and the lines (which are difficult to individually distinguish) are 95 % confidence intervals. The black vertical lines are the true values, and the numbers to the right are the proportion of confidence intervals that bracket the true value, the target being 0.95. The 4th simulation scenario is not presented because there is not a single true value. Tick marks refer to the same values in all graphs.

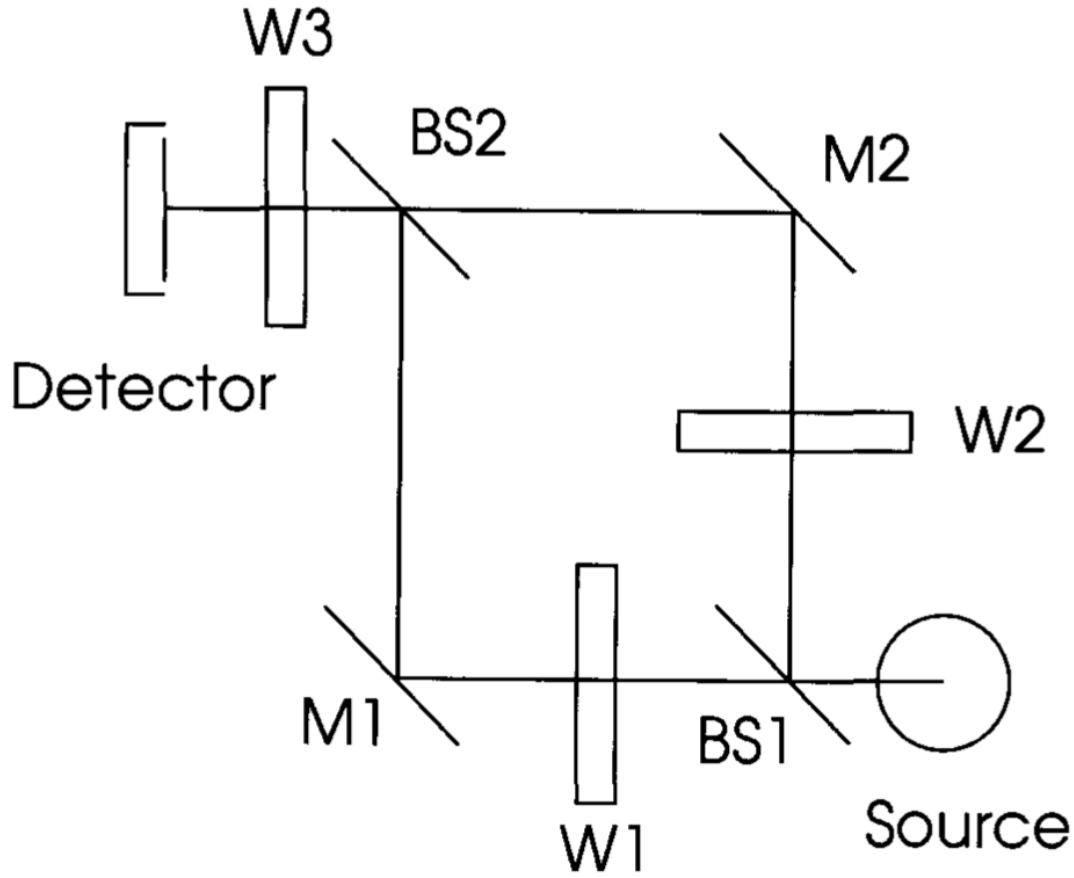


Figure 4: Schematic diagram of the Beam Conjoiner showing the primary elements. BS: beam splitter; W: filter wheel; and M: mirror. The schematic is taken from [2].

wheel before being viewed by the instrument. The filter combinations enable a dynamic range of signals of about 500 in a single measurement scan of all of the combinations. Additional ranges are achieved using an external neutral density filter wheel which then can be used to obtain a dynamic range of 14 orders of magnitude [14]. A schematic of the beam conjoiner is given in Figure 4.

The methodology of Section 2 may not be applied exactly as prescribed there because the true light intensity viewed by the detector for experimental run i is not naturally written as $\Phi_i = \sum_{j=1}^J x_{ij} \phi_j$ as in Equation (1). Recall that x_{ij} indicates lamp j being off/on in experimental run i . For the Beam Conjoiner, the true light intensity viewed by the instrument for experimental run i may be written as $\Phi_i = \sum_{j_1=1}^{J_1} x_{1ij_1} \phi_{1j_1} + \sum_{j_2=1}^{J_2} x_{2ij_2} \phi_{2j_2}$. Here, ϕ_{1j_1} represents the flux contributed by beam 1 after it passes through combination j_1 of the two filters that it passes through before being viewed by the detector. A similar interpretation holds for ϕ_{2j_2} for beam 2. The labels “beam 1” and “beam 2” are arbitrary and interchangeable and represent light that has passed through either of the two paths within the beam conjoiner. Each

variable x_{1ij_1} or x_{2ij_2} takes on the values 0 and 1. Together they represent specific setting combinations for the filters that beams 1 and 2 pass through, respectively. There are J_1 and J_2 settings associated with beams 1 and 2, respectively. For experimental run i , no more than one of $(x_{1i1}, \dots, x_{1iJ_1})$ may be one, but they may all be zero to indicate no flux contribution. The same constraint is true for $(x_{2i1}, \dots, x_{2iJ_2})$.

A second modification of the methodology of Section 2 is needed for the Beam Conjoiner. In Equation (1), the electronic noise is represented by the parameter σ , which is assumed to be constant across experimental runs. For the data from the Beam Conjoiner experiments, it is clear that the electronic noise increases with flux. As a result, σ from Equation (1) becomes σ_i , and for the current application, σ_i takes the form

$$\sigma_i = \begin{cases} \sigma\Phi_i & \text{if } \Phi_i > \kappa_0\Phi_{\max} \\ \sigma\kappa_0\Phi_{\max} & \text{if } \Phi_i \leq \kappa_0\Phi_{\max}. \end{cases} \quad (4)$$

In Equation (4), the electronic noise is assumed constant until the flux exceeds $\kappa_0\Phi_{\max}$, and after that it is assumed proportional to the flux. In practice, κ_0 must be chosen, which in this case was done by inspecting residuals after fitting the constant noise model. The value $\kappa_0 = 0.2$ was selected here.

It is also necessary to choose the polynomial degree p . The typical approach to choosing such a model parameter is to balance the trade-off between prediction variance and bias. As p increases, so too does the prediction variance, but prediction bias simultaneously decreases.

The strategy K -fold cross validation (see for example Chapter 5 of [15]) minimizes an estimate of the sum of the prediction variance and squared bias, i.e., mean squared error (MSE). Other common strategies, like applying the Akaike information criterion (AIC) [16] or the Bayesian information criterion (BIC) [17] achieve similar goals, but are derived from different foundations.

The likelihood in Equation (2), attempts to balance the bias-variance trade-off automatically through the parameter γ . As γ approaches zero, α_1 approaches $\frac{1}{2}\Phi_{\max}$ and the α_m for $m = 2, \dots, p$ approach zero. In this limit, variance is minimized (zero variance), but bias is maximized. Conversely, as γ approaches ∞ , bias is minimized, but variance is maximized. By estimating γ along with the other parameters, the two extremes are balanced. This implies that p should be chosen to be very large to allow bias and thus mean squared error to be minimized, and that minimization is part of the estimation process. If p is too small, the bias will be artificially inflated.

Practically, however, p cannot be chosen to be arbitrarily large. A range of values of p producing an optimal and stable MSE may be identified by K -fold cross validation. Figure 5 shows the results of 10-fold cross validation using the Beam Conjoiner data. For each polynomial degree, there are 10 estimates of MSE corresponding to the 10 folds (random splits of the data). Because the MSE is being automatically balanced by the parameter γ in Equation (2), a level horizontal band is expected and found in Figure 5. For $8 \leq p \leq 15$, the distributions of points (blue circles) and means (orange circles) are

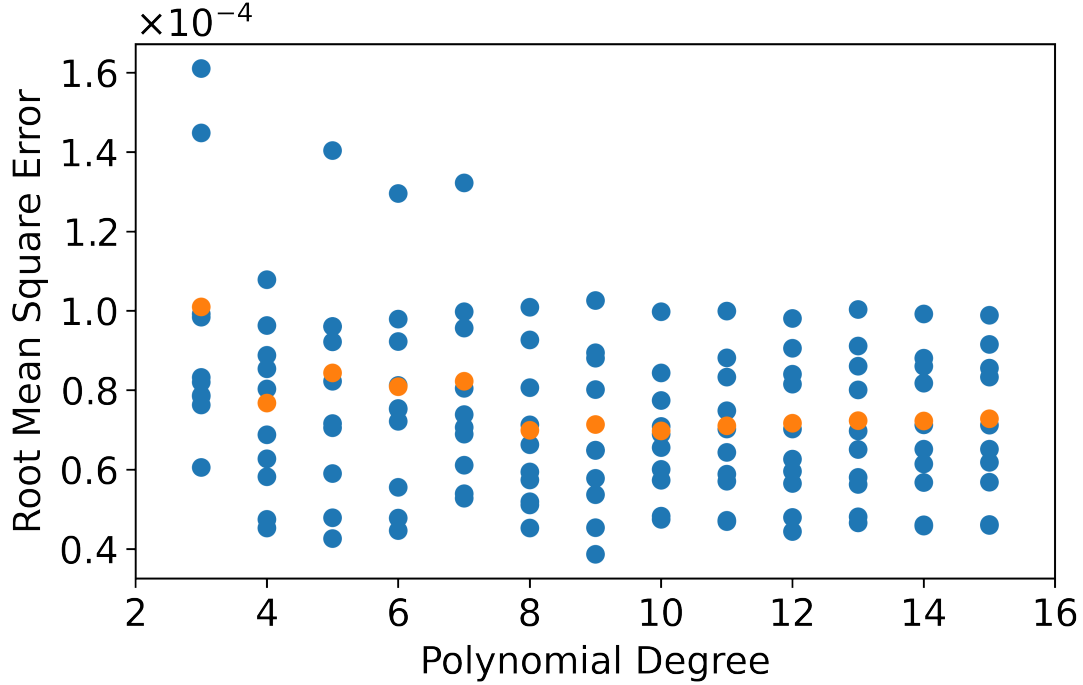


Figure 5: The 10-fold cross validation error plotted as a function of the polynomial degree p for the Beam Conjoiner data discussed in Section 4. For each polynomial degree, the 10 estimates of root mean squared prediction error (MSE) are plotted (blue circles) as well as the square root of the average MSE (orange circles).

nearly identical; although, the minimum mean is achieved for $p = 10$. Based on Figure 5, any p in the range of $8 \leq p \leq 15$ is a reasonable choice.

The values of MSE in Figure 5 may be interpreted in the following way: when p is small, prediction bias dominates the MSE. As p increases, prediction bias decreases, and the γ parameter in Equation (2) automatically balances the trade off between prediction bias and variance, which produces a range of p for which the MSE is optimal and stable.

4.1. Results

Figure 6 plots the residuals $n_i - \hat{\alpha}_0 - \sum_{m=1}^p \hat{\alpha}_m P_m(s(\hat{\Phi}_i))$ on the vertical axis versus the estimated fluxes $\hat{\Phi}_i$ on the horizontal axis. The increasing electronic noise with flux is apparent. The residuals at each estimated flux level are symmetrically distributed around zero. This implies that the model described in Equation (1), with the modifications detailed above, represents the Beam Conjoiner data well. The light red band in Figure 6 depicts 95 % pointwise prediction bounds for the residuals. The target 95 % coverage of the prediction bounds is achieved. This implies that the bootstrapping pairs algorithm properly accounts for uncertainty in the estimated model parameters and that the model for the electronic noise in Equation (4) is appropriate. The light

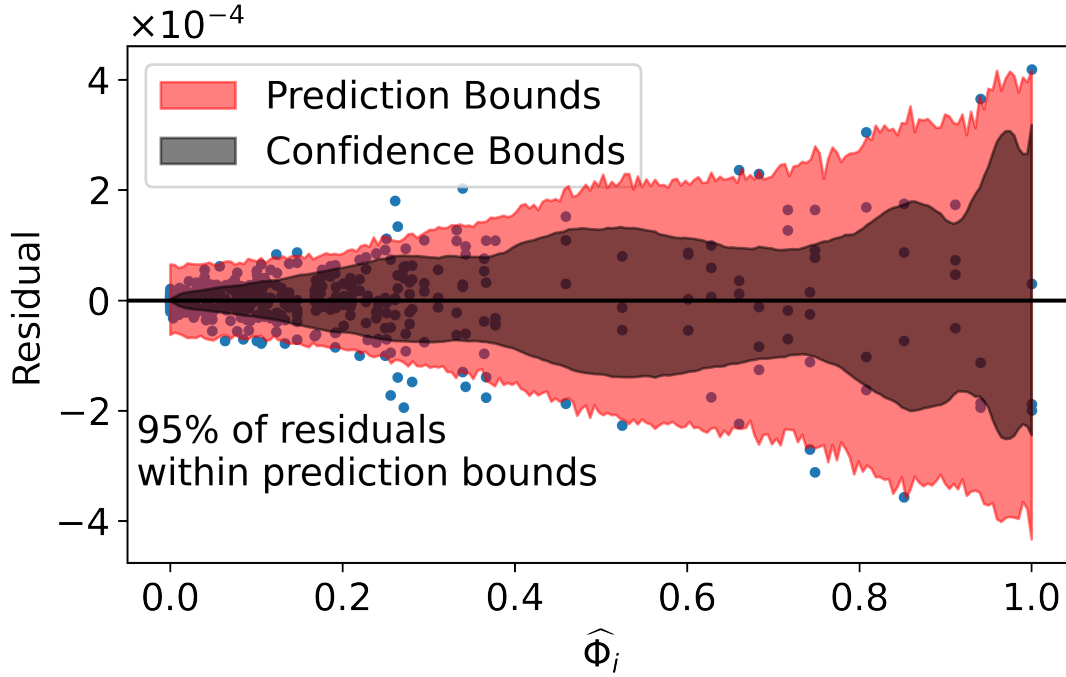


Figure 6: Residuals versus the estimated fluxes (blue points), 95 % pointwise prediction bounds for the residuals (light red band), and 95 % pointwise confidence bounds for the mean residual.

grey band in Figure 6 depicts 95 % pointwise confidence bounds for the mean residual. By construction the band contains zero, but at higher flux values and those where there are fewer observed data, the bands widen indicating more uncertainty in the average residual.

Figure 7 shows the estimated nonlinear detector response where the horizontal axis represents flux and the vertical axis the detector response; the dashed green line is the diagonal, the black curve is the estimated mean detector response, and the red points are instrument readings, n_i . Note that in Figure 7 the deviation between the diagonal and the estimated mean detector response has been exaggerated; otherwise, visually, the curves are indistinguishable. Figure 8 shows the estimated non-linear response in a different way, depicting differences between the estimated expected detector response and the diagonal (black curve), bootstrap replicates of that difference (blue curves), and differences between the the observed detector responses and the diagonal (red points); the diagonal in Figure 7 becomes a horizontal line at zero in Figure 8. No exaggeration for visual effect is needed in Figure 8. There are 982 bootstrap replicates shown because 18 of the attempted 1000 bootstrap replicates encountered failures in optimization of the likelihood function given in Equation (2) (modified appropriately based on the discussion of this section, 4). The Beam Conjoiner exhibits statistically significant nonlinear behavior because in Figure 8 the bootstrap replicates do not envelop

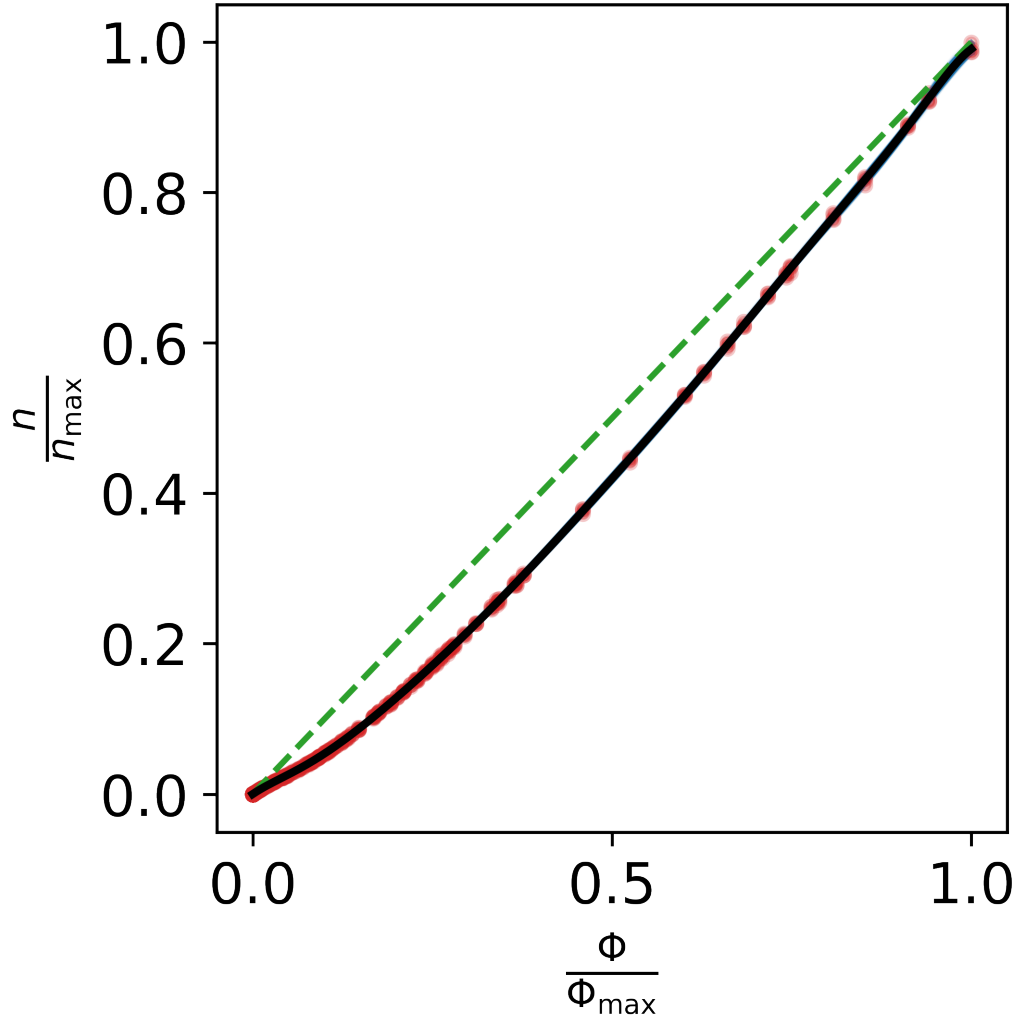


Figure 7: The horizontal axis depicts the flux, and the vertical axis depicts the instrument reading. The black curve is the MLE of the expected instrument reading. The red points depict the observed n_i . The deviation between the expected detector response and the (green dashed) 1:1 diagonal are exaggerated by a factor of 25; otherwise, the curves would be visually indistinguishable.

zero. The orange curve in Figure 8 will be discussed in the next section, 4.2.

4.2. Comparison to an Existing Approach

The approach to estimating β_0, \dots, β_p , $\phi_{11} \dots \phi_{1J_1}$, and $\phi_{21}, \dots, \phi_{2J_2}$ from [2] is based on optimizing a least-squares-like objective function. In comparison to the likelihood

function in Equation (2), but using similar notation, it is

$$\left[\Phi_{\max} - \max_i \{ \Phi_i \} \right]^2 + \sum_{i=1}^N \left[\left(\beta_0 + \sum_{m=1}^p \beta_m n_i^m \right) - \Phi_i \right]^2. \quad (5)$$

There are several differences between this objective function and the likelihood function in Equation (2), but most notably it is not derived from a generative probability model as the likelihood function in Equation (2) is derived from Equation (1). We consider it to be a best practice when making inferences from data to begin with a generative probability model, and indeed it is a requirement in the two major paradigms of statistical inference, maximum likelihood and Bayesian inference. It is possible to apply Bayesian methods to the model in Equation (1) even though we choose to use maximum likelihood. Other differences include that there is no explicit mechanism for mapping flux to the expected detector signal, and there is no explicit mechanism to handle the increased spread in the residuals apparent in Figure 6.

Figure 8 also includes an estimate of detector nonlinearity based on minimizing Equation (5) (orange curve). Clearly, the two procedures produce similar results since both estimates of detector nonlinearity fall nearly on top of each other. The largest differences are found at high values of flux where there is more distinction between the approaches since the maximum likelihood approach of this work accounts for increasing variability in the detector response as flux increases. The estimate of nonlinearity based on Equation (5) is also completely within the range of the bootstrap replicates of the estimated nonlinearity based on Equation (1) (light blue curves). These observations provide further confidence in the proposed approach. Both approaches produce similar estimates of the nonlinear behavior of the detector, but the approach proposed within adds flexibility and rigorous confidence and prediction intervals that may be used to express uncertainty in the results.

4.3. Calibration

Linearizing the instrument response is not sufficient to translate observations from an instrument to fluxes because it is only possible to do so up to an arbitrary scale. A further calibration step is necessary. Suppose that for a reference flux Φ_{ref} , known for practical purposes without uncertainty, the average detector response, $E[n_{\text{ref}}]$ is also known for practical purposes without uncertainty. Using Equation (3) and the MLE $\hat{\beta}$,

$$\hat{\Phi}_{\text{ref}} = \hat{\beta}_0 + \sum_{m=1}^p \hat{\beta}_m E[n_{\text{ref}}]^m$$

is obtained. With the bootstrap replicates $\{\beta^{*,b}\}_{b=1}^B$, $\{\Phi_{\text{ref}}^{*,b}\}_{b=1}^B$ are similarly obtained. The ratios $\hat{\rho} = \frac{\Phi_{\text{ref}}}{\hat{\Phi}_{\text{ref}}}$ and $\rho^{*,b} = \frac{\Phi_{\text{ref}}}{\Phi_{\text{ref}}^{*,b}}$ provide single point calibrations. When a new detector observation, n , is made, it is translated to a calibrated flux as

$$\hat{\Phi}_{\text{cal}} = \hat{\rho} \left[\hat{\beta}_0 + \sum_{m=1}^p \hat{\beta}_m n^m \right].$$

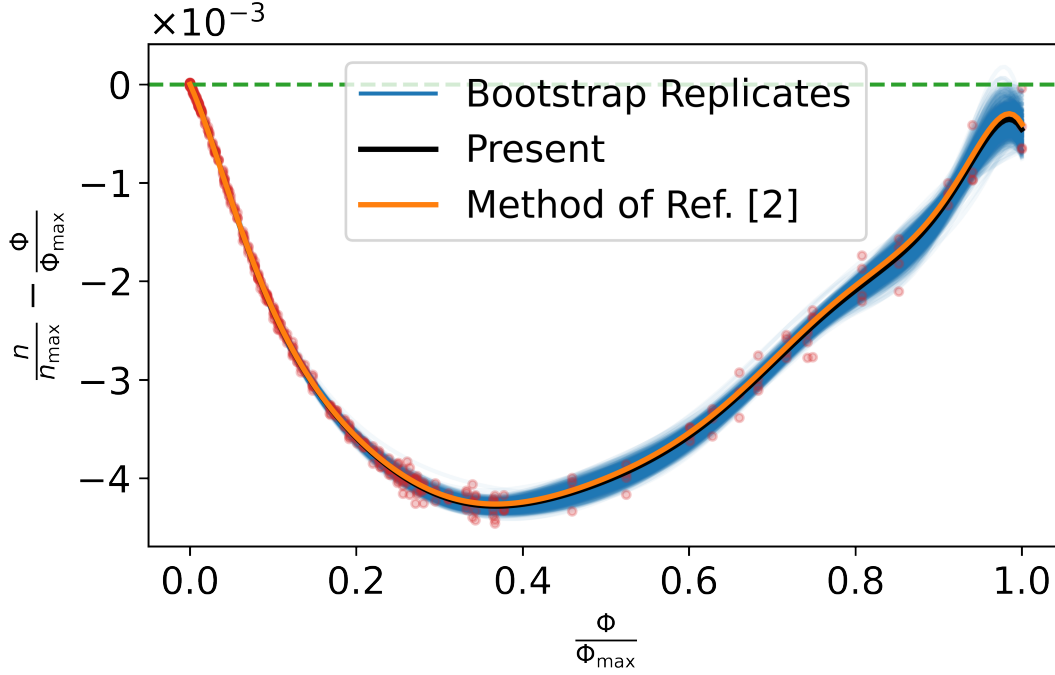


Figure 8: The horizontal axis depicts the flux, and the vertical axis depicts the instrument reading minus the flux. The black curve is the estimated expected instrument reading minus the flux where the estimated expected instrument reading is calculated by the methods described in the present work. The blue curves are bootstrap replicates (as described in the present work) of the estimated expected instrument reading minus the flux. The red points depict n_i minus the estimated flux for experimental run i , $\hat{\Phi}_i$ where the estimated expected instrument reading is calculated by the methods described in the present work. The orange curve is an estimate of the expected instrument reading minus the flux based on Equation (5) and [2].

Bootstrap replicates $\{\Phi_{\text{cal}}^{*,b}\}_{b=1}^B$, to quantify uncertainty, are similarly obtained. When $n = E[n_{\text{ref}}]$ the calibrated value is Φ_{ref} , and all of the bootstrap replicates are identically Φ_{ref} . Uncertainty in Φ_{ref} may be considered separately from uncertainty in the estimate of nonlinearity.

Figure 9 shows the results of this calibration for the Beam Conjoiner data assuming $E[n_{\text{ref}}] = 0.5$ and $\Phi_{\text{ref}} = 0.5$, which is chosen because indicating instruments are generally designed to perform well at midrange. In Figure 9a, the vertical axis displays $\Phi_{\text{cal}}^{*,b} - \hat{\Phi}_{\text{cal}}$ and the horizontal $\hat{\Phi}_{\text{cal}}$. The pinching of the curves to the value zero in Figure 9a happens at $\hat{\Phi}_{\text{cal}} = \Phi_{\text{ref}} = 0.5$. Figure 9b displays the relative differences instead of the absolute differences. It may be seen directly in Figure 9b, that for most of the range of $\hat{\Phi}_{\text{cal}}$, the $\{\Phi_{\text{cal}}^{*,b}\}_{b=1}^B$ are within 0.025 % of $\hat{\Phi}_{\text{cal}}$. This may be interpreted as the contribution of uncertainty attributable to empirical estimation the linearization function.

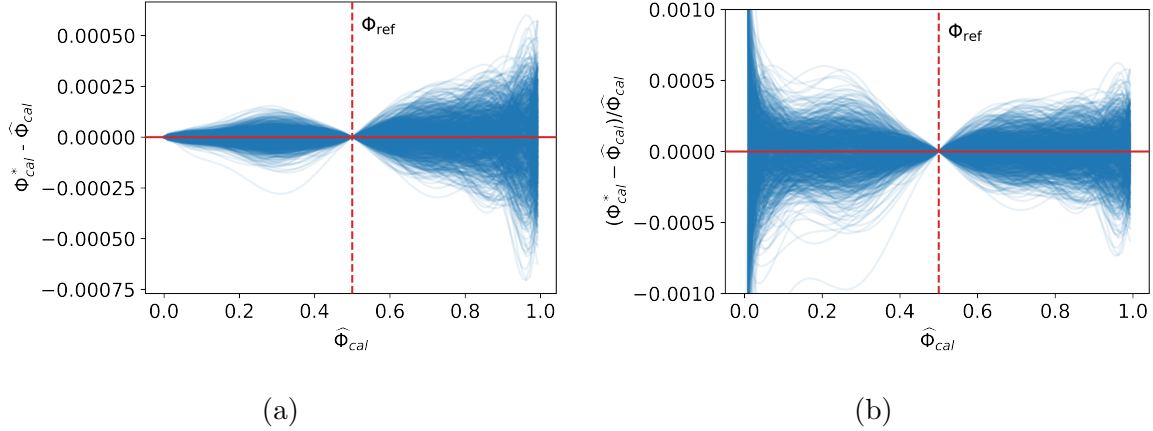


Figure 9: In both figures, the horizontal axis depicts the MLEs of calibrated fluxes, $\hat{\Phi}_{cal}$. In (a) the vertical axis depicts bootstrap replicates of MLEs of calibrated fluxes minus MLEs of calibrated fluxes. Each curve represents a single bootstrap replica. The vertical axis in (b) is similar, but the relative difference is plotted.

5. Summary

This article investigates the problem of quantifying uncertainty when applying the radiometry technique known as the flux-addition method. There are four primary novel contributions:

- (i) A generative probability model applicable to the calibration of radiometers is introduced. This permits the application of maximum likelihood.
- (ii) A non-parametric bootstrap algorithm is described for the purpose of making uncertainty statements about estimates of the parameters of the probability model.
- (iii) The coverage probabilities of confidence intervals derived from the bootstrap algorithm are assessed via simulation.
- (iv) The probability model requires the choice of a polynomial degree. A cross-validation based strategy is proposed to help make that choice.

The probabilistic model and bootstrap algorithm were tested in a simulation study. The simulation study was guided by experience in calibrating the Orbiting Carbon Observatory-2. In the simulation study, the MLEs for the polynomial coefficients of the linearizing function were found to be approximately unbiased, meaning when estimates are averaged across many data sets, the average value is approximately the true value. For the polynomial coefficients defining the linearization function, the relative bias observed in the simulation study was less than 1 %. The simulation study also shows that bootstrap percentile confidence intervals for the same polynomial coefficients are consistent with their nominal 95 % coverage. In 100 simulations, the observed coverage proportions ranged from 90 % to 97 %. Similar results were obtained for the other model parameters, e.g., fractional flux factors for variable aperture lamps. The coverage results

held for some model parameters, most notably β , even when the model assumption of constant lamp fluxes, over the duration of the experiment, was relaxed. We note that to use the methodology on a real satellite instrument would require careful planning to ensure that the measurements and the model are well-matched.

The probabilistic model and bootstrap algorithm were also tested on an experimental data set from the NIST Beam Conjoiner. For those data it was necessary to modify the probabilistic model for the integrating sphere in two ways: (1) the flux presented to the instrument for each experimental run was the sum of exactly two fluxes, one contributed by each beam; and (2) the electronic noise was allowed to increase proportionally with flux. The model was deemed to perform well for these data because pointwise 95 % prediction intervals for the residuals enveloped exactly 95 % of them. After a further calibration step, for the Beam Conjoiner data set, the component of uncertainty in a calibrated value, attributable to estimation of the linearizing function, was found to be less than 0.025 % for most of the range of the instrument. The method provides unbiased estimates for nonlinear corrections required in high-precision calibrations along with accurate uncertainty statements.

Acknowledgements

The authors thank Robert Rosenberg of NASA Jet Propulsion Laboratory for helpful conversations and feedback.

Disclaimers

Certain commercial products or company names are identified here to describe our study adequately. Such identification is not intended to imply recommendation or endorsement by the National Institute of Standards and Technology, nor is it intended to imply that the products or names identified are necessarily the best available for the purpose. The manuscript is a product of the United States Government and not subject to copyright in the United States

Appendix A. Table of Symbols

Table A1: Table of symbols. If a symbol appears in the *Integrating Sphere* section, it is not repeated in the following sections, e.g., Φ_i . With the exception of symbols appearing in the calibration section, accented symbols, such as $\hat{\alpha}_0$, are not included because the accent does not change the underlying meaning of the symbol. For $\hat{\alpha}_0$, the accent designates that it is the MLE of the unaccented symbol. The meaning of all accents are discussed at first use. In the calibration section, some symbols are originally defined with accents.

n_i	Instrument reading for experimental run $i = 1, \dots, N$.
n	General symbol denoting an instrument reading.
N	Number of instrument readings.
α_m	Legendre polynomial coefficients; $m = 1, \dots, p$.
p	Maximum polynomial degree.
$P_m(\cdot)$	Legendre polynomial of order m .
$s(\cdot)$	Function that shifts and scales inputs to the interval $[-1, 1]$.
Φ_i	Stimulus for experimental run i .
Φ	General symbol denoting a stimulus for an experimental run.
σ	Standard deviation of electronic noise.
ϕ_j	Flux for lamp $j = 1, \dots, J$.
x_{ij}	Indication of lamp j being 0 (off) or 1 (on) for experimental run i .
Φ_{\max}	Estimate of maximum flux.
τ	Uncertainty in estimated maximum flux expressed as a standard deviation.
γ	Shrinkage parameter for the Legendre polynomial coefficients, similar to the corresponding quantity in ridge regression.
λ	Prior expected value of the shrinkage parameter; we choose Φ_{\max} for this value.
ψ_k	Scale in $[0, 1]$ for variable aperture setting $k = 1, \dots, N_v$.
x_{iJk}	Indication 0 (not used) or 1 (used) of variable aperture state k for experimental run i .
N_v	Number of variable aperture settings.
β_m	Polynomial coefficients defining the linearization function.
Beam Conjoiner	
ϕ_{1j_1}	Flux contributed by beam 1 for filter combination j_1 .
ϕ_{2j_2}	Flux contributed by beam 2 for filter combination j_2 .
x_{1ij_1}	Indication of filter combination j_1 for experimental run i (0 or 1).
x_{2ij_2}	Indication of filter combination j_2 for experimental run i (0 or 1).
σ_i	Standard deviation of electronic noise for experimental run i .
κ_0	The cutoff below which electronic noise is assumed constant is $\kappa_0 \Phi_{\max}$.
σ	The standard deviation of the electronic noise is assumed to be proportional to the flux with proportionality constant σ .
Calibration	
Φ_{ref}	Reference flux.
$E[n_{\text{ref}}]$	Expected instrument response at Φ_{ref} .
$\hat{\Phi}_{\text{ref}}$	Linearized response at Φ_{ref} .
$\hat{\rho}$	Calibration ratio (for single point calibration).
$\hat{\Phi}_{\text{cal}}$	Calibrated flux.

References

- [1] White D R, Clarkson M T, Saunders P and Yoon H W 2008 *Metrologia* **45** 199–210
 ISSN 0026-1394 URL <https://doi.org/10.1088%2F0026-1394%2F45%2F2%2F009>

- [2] Thompson A K and Chen H M 1994 *J. Res. Natl. Inst. Stand. and Technol.* **99** 751–755
- [3] Shin D J, Park S, Jeong K L, Park S N and Lee D H 2013 *Metrologia* **51** 25–32
- [4] Legendre and related functions, Chap. 14 in the *NIST Digital Library of Mathematical Functions* <http://dlmf.nist.gov/>, Release 1.1.3 of 2021-09-15, F. W. J. Olver, A. B. Olde Daalhuis, D. W. Lozier, B. I. Schneider, R. F. Boisvert, C. W. Clark, B. R. Miller, B. V. Saunders, H. S. Cohl, and M. A. McClain, eds. URL <http://dlmf.nist.gov/14>
- [5] Wood S 2015 *Core Statistics* (Cambridge University Press) ISBN 9781107071056
- [6] Hoerl A E and Kennard R W 1970 *Technometrics* **12** 55–67
- [7] Tibshirani R 1996 *Journal of the Royal Statistical Society: Series B (Methodological)* **58** 267–288
- [8] Gelman A, Carlin J, Stern H, Dunson D, Vehtari A and Rubin D 2013 *Bayesian Data Analysis, Third Edition* Chapman & Hall/CRC Texts in Statistical Science (Taylor & Francis) ISBN 9781439840955
- [9] Park T and Casella G 2008 *Journal of the American Statistical Association* **103** 681–686
- [10] Rosenberg R, Maxwell S, Johnson B C, Chapsky L, Lee R A M and Pollock R 2017 *IEEE Transactions on Geoscience and Remote Sensing* **55** 1994–2006 ISSN 0196-2892
- [11] Rosenberg R, Maxwell S, Johnson B C, Chapsky L, Lee R A and Pollock R 2017 *IEEE Transactions on Geoscience and Remote Sensing* **55** 1994–2006
- [12] Efron B and Tibshirani R J 1993 *An Introduction to the Bootstrap* (CRC press)
- [13] Markham B, Barsi J, Kvaran G, Ong L, Kaita E, Biggar S, Czaplak-Myers J, Mishra N and Helder D 2014 *Remote Sensing* **6** 12275–12308 ISSN 2072-4292 URL <https://www.mdpi.com/2072-4292/6/12/12275>
- [14] Eppeldauer G and Hardis J E 1991 *Applied Optics* **30** 3091–3099
- [15] James G, Witten D, Hastie T and Tibshirani R 2013 *An Introduction to Statistical Learning: with Applications in R* Springer Texts in Statistics (Springer New York) ISBN 9781461471387
- [16] Akaike H 1974 *IEEE Transactions on Automatic Control* **19** 716–723
- [17] Schwarz G 1978 *The Annals of Statistics* 461–464